

Extreme Antiscaling Performance of Slippery Omniphobic Covalently Attached Liquids

Hanyang Zhao, Chirag Anand Deshpande, Longnan Li, Xiao Yan, Muhammad Jahidul Hoque, Gowtham Kuntumalla, Manjunath C Rajagopal, Ho Chan Chang, Yuquan Meng, Sreenath Sundar, Placid Ferreira, Chenhui Shao, Srinivasa Salapaka, Sanjiv Sinha, and Nenad Miljkovic*

Cite This: *ACS Appl. Mater. Interfaces* 2020, 12, 12054–12067

Read Online

ACCESS |

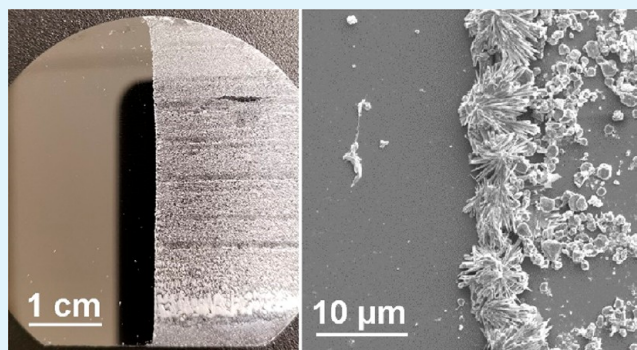
Metrics & More

Article Recommendations

Supporting Information

ABSTRACT: Scale formation presents an enormous cost to the global economy. Classical nucleation theory dictates that to reduce the heterogeneous nucleation of scale, the surface should have low surface energy and be as smooth as possible. Past approaches have focused on lowering surface energy via the use of hydrophobic coatings and have created atomically smooth interfaces to eliminate nucleation sites, or both, via the infusion of low-surface-energy lubricants into rough superhydrophobic substrates. Although lubricant-based surfaces are promising candidates for antiscaling, lubricant drainage inhibits their utilization. Here, we develop methodologies to deposit slippery omniphobic covalently attached liquids (SOCAL) on arbitrary substrates. Similar to lubricant-based surfaces, SOCAL has ultralow roughness and surface energy, enabling low nucleation rates and eliminating the need to replenish the lubricant. To enable SOCAL coating on metals, we investigated the surface chemistry required to ensure high-quality functionalization as measured by ultralow contact angle hysteresis ($<3^\circ$). Using a multilayer deposition approach, we first electrophoretically deposit (EPD) silicon dioxide (SiO_2) as an intermediate layer between the metallic substrate and SOCAL. The necessity of EPD SiO_2 is to smooth (<10 nm roughness) as well as to enable the proper surface chemistry for SOCAL bonding. To characterize antiscaling performance, we utilized calcium sulfate (CaSO_4) scale tests, showing a 20 \times reduction in scale deposition rate than untreated metallic substrates. Descaling tests revealed that SOCAL dramatically decreases scale adhesion, resulting in rapid removal of scale buildup. Our work not only demonstrates a robust methodology for depositing antiscaling SOCAL coatings on metals but also develops design guidelines for the creation of antifouling coatings for alternate applications such as biofouling and high-temperature coking.

KEYWORDS: fouling, wetting, SOCAL, SLIPS, LIS, interface, salt, hydrophobic



INTRODUCTION

Scaling is a major unresolved problem in a variety of industries including water treatment^{1,2} and power generation.^{3,4} In heat exchangers, accumulation of salt scale on surfaces can lead to decreased heat transfer, increased corrosion, and increased pressure drop, resulting in higher operational costs and shortened equipment lifetime.⁵ The added operational costs for active scale removal such as mechanical abrasion and chemical inhibition account for 0.25% of the gross domestic product and 2.5% of the CO_2 emissions in industrialized nations.⁶ In the past few decades, an emphasis has been placed on developing techniques to enable scale mitigation. These efforts have mostly focused on improving the efficiency of mechanical and chemical removal techniques.^{7,8}

Many detailed studies of scaling phenomena have been conducted in the past.^{9,10} Recent methods have proposed altering the surface structure and chemistry to control the heterogeneous nucleation rate of scale formation.^{10–13} Accord-

ing to classical nucleation theory,¹⁴ lowering the surface energy of the substrate increases the energy barrier for heterogeneous nucleation and thus leads to delayed salt scaling. Furthermore, surfaces that are rendered ultrasmooth or atomically smooth provide fewer sites for heterogeneous nucleation, leading to reduced scaling rates.^{11,12} A promising method to achieve simultaneous reduction in surface energy and roughness is through the fabrication of slippery liquid infused porous surfaces (SLIPSs)¹⁵ or lubricant infused surfaces (LISs).^{16,17} Both SLIPSs and LISs require surface structuring and lubricant

Received: December 6, 2019

Accepted: February 11, 2020

Published: February 11, 2020

infusion to achieve low-surface-energy and atomically smooth interfaces.¹⁸ The main drawback of SLIPs and LISs is their propensity to degrade over time due to lubricant drainage, especially in applications where single-phase flow is present,^{19,20} common in many applications where scaling occurs.

In order to mitigate lubricant drainage, we study slippery omniphobic covalently attached liquids (SOCAL) as a means to achieve durable antiscaling performance on metallic substrates. The SOCAL coating has great potential for antiscaling performance due to its ultralow surface energy and high topographical homogeneity.²¹ Here, we develop and demonstrate multiple methods to deposit SOCAL coatings on arbitrary surfaces through the use of spin-on-glass (SOG), physical vapor deposition (PVD) of SiO₂, and electrophoretic deposition (EPD) of SiO₂ as an intermediary layer between the arbitrarily shaped substrate and the coating.^{22–24} The use of previously developed EPD recipes resulted in rough surface finishes, not suitable for antifouling applications due to the need for topographical homogeneity. To achieve smoother SiO₂ EPD coatings, we lowered the concentration of tetraethyl orthosilicate (TEOS) and added triethoxymethylsilane (MTES) to the EPD solution. Scanning electron and atomic force microscopy demonstrated ultrasmooth and structurally homogeneous interfaces of EPD SiO₂ on metallic substrates. To characterize surface chemistry, we used Lifshitz–van der Waals (LW) theory²⁵ to demonstrate interfacial energies of 11.17 mJ/m² at the SOCAL–liquid interface. To characterize antiscaling performance, we conducted scaling and descaling tests using CaSO₄, demonstrating a 95% reduced scaling rate when compared to that of bare polished aluminum (Al) surfaces. Furthermore, our tests revealed that SOCAL coated Al has enhanced descaling rates compared to results for untreated polished Al due to the ultralow adhesion of the nucleated scale to the SOCAL interface. Our work not only develops a scalable manufacturing technique capable of easily applying SOCAL coatings on metallic substrates but also demonstrates SOCAL as a passive fouling mitigation technique in salt-scaling applications.

METHODS

Silicon Wafer Preparation and SOCAL Coating. The SOCAL coating methodology was adopted from previous work.²¹ The SOCAL coating was originally designed for deposition on polished Si wafers using dip coating. The SOCAL solution consisted of a room temperature mixture of 100:10:1 wt % isopropanol (IPA, CAS Registry No.: 67-63-0, Sigma-Aldrich), dimethyldimethoxysilane (DMDMS, CAS Registry No.: 1112-39-6, Sigma-Aldrich), and sulfuric acid (CAS Registry No.: 7664-93-9, Sigma-Aldrich). We began by adding DMDMS into IPA, followed by the addition of sulfuric acid in a cleaned and dry glass beaker. Once all chemicals were added to the beaker, we vigorously stirred the solution using a glass stick by hand for 30 s. After stirring, the solution was allowed to rest in a capped glass container for at least 20 min prior to use. The Si wafer was then vigorously rinsed for 30 s each in deionized water (DI water, CAS Registry No.: 7732-18-5, Sigma-Aldrich), IPA, and acetone (CAS Registry No.: 67-64-1, Sigma-Aldrich) and then again in IPA. Immediately after rinsing, the Si wafer was dried in a clean nitrogen gas (N₂) stream. After drying, air plasma cleaning (HDC-001-HC, Harrick-Plasma) was performed at high power for 5 min to remove any remaining organic residue from the Si wafer surface. The cleaned Si wafer was then submerged in the quiescent SOCAL solution for 5–10 s and withdrawn gradually at a rate of ≈ 2 cm/s by hand. After removal, the edge of the sample was contacted gently with an absorbent paper towel (Brawny H700) to remove any excess solution via wicking, followed by leaving the sample to reside at room temperature for 20 min

to ensure drying. Next, the sample was cleaned again using vigorous rinsing for 10 s each in DI water, IPA, toluene (CAS Registry No.: 108-88-3, Sigma-Aldrich), and again IPA. Finally, the sample was blown dry with a clean N₂ stream.

Application of the SOCAL coating on polished 6061 Al substrates (McMaster, 1651T3) utilizing the aforementioned recipe developed for Si wafers resulted in poor coating performance. The coating efficacy was measured by the resulting water droplet contact angle hysteresis, defined as the difference between the apparent advancing and receding contact angles, which for successful SOCAL coating should not exceed 3°. When the same recipe was applied to polished Al samples, the resulting contact angle hysteresis exceeded 10°, indicating coating failure. To test whether roughness or surface chemistry were factors in coating failure, we sputter deposited a thin (≈ 200 nm) layer of Al on a clean polished Si wafer and then repeated the aforementioned SOCAL coating method. Coating of SOCAL on an ultrasmooth mirror-finish Al interface yielded results similar to those on bulk polished Al samples, mainly the unsuccessful deposition of SOCAL. We hypothesize that the difference in hydroxyl group density of pristine SiO₂ interfaces compared to AlO(OH) interfaces results in the coating difference. This difference is also responsible for the varying volatile organic compound dynamics that different metal oxides display.^{26,27} Indeed, the main factors to influence surface modification are the concentration of surface hydroxyl groups, the type of surface hydroxyl groups present at the interface, the hydrolytic stability of the bond formed between the groups and the SOCAL molecules, and geometry and physical dimensions of the substrate.²⁸ Hydroxyl-containing substrates vary widely in concentration and type of hydroxyl groups present, with glass or silica being two of the best substrate materials for surface modification in comparison to Al.^{29–32} Given this result, we deposit SiO₂ on Al substrates prior to SOCAL coating. This forms a sandwich structure with three layers (Al–SiO₂–SOCAL); the SiO₂ layer is deposited by different methods. On all intermediate layers, EPD, PVD, and SOG, the silane concentration was doubled; i.e., the SOCAL solution used for these samples is a mixture of 100:20:1 wt % isopropanol, dimethyldimethoxysilane, and sulfuric acid. Doubling of the silane concentration was done since the original recipe used a polished Si wafer as the substrate, which was atomically smooth. Since some roughness was present on our fabricated samples, we attempted to increase the silane dosage in case the initial recipe lacked the concentration to achieve full coverage.

Aluminum Sample Preparation and Electrophoretic Deposition (EPD). Aluminum tabs (Polished 6061 Al, McMaster) were cut in 2.5 cm \times 8 cm \times 0.2 cm sizes on a conventional mill. After cutting, the protective adhesive tape on the polished side was peeled off, resulting in remnants of adhesive residue. To remove the adhesive residue, a commercial grease remover (Orange Blast, Greased Lightning) was used. Briefly, the Al tabs were sprayed with the grease remover, followed by vigorous rubbing on the polished surface using a soft sponge (Nonscratch, Scotch Bright), followed by vigorous rinsing in room-temperature laboratory tap water. The samples were then rinsed for 10 s in DI water, followed by IPA, followed by N₂ drying and air plasma cleaning at high power for 5 min as described above.

The original EPD recipe was adopted from past literature²⁴ where the molar ratio of TEOS:water:ethanol was 0.2:10:10, respectively. The water was adjusted to pH = 11.7 by the addition of NH₄OH. This recipe is herein referred to as the “initial recipe”. Our modified recipe was prepared as follows. We started by making EPD solvent using a 1:1 molar ratio of DI water and ethanol (CAS Registry No.: 64-17-5, Sigma-Aldrich). Prior to mixing the solvent, the DI water was modified to a pH of 13 by adding sodium hydroxide (NaOH, CAS Registry No.: 1310-73-2, Sigma-Aldrich) and vigorously mixing at room temperature using a glass stick to dissolve the NaOH. The EPD solute was made using a 1:1 molar ratio of tetraethyl orthosilicate (TEOS, CAS Registry No.: 78-10-4, Sigma-Aldrich) and triethoxymethylsilane (MTES, CAS Registry No.: 2031-67-6, Sigma-Aldrich). The molar ratio of solvent and solute is 19:1. The final molar ratio is water:ethanol:TEOS:MTES was 19:19:1:1. The TEOS and MTES were mixed in a glass beaker by with a PTFE stir bar on hot plate rotating at 200 rpm. The entire beaker with solute was kept in an ice water bath in order to maintain a

temperature of 0 °C. The solvent was then slowly added to the solute with continual stirring by the PTFE stir bar. The complete solution was kept in the ice bath during the entire EPD procedure.

After the polished Al sample was cleaned by air plasma, it was immediately (within 30 s) placed in the EPD solution as the anode. A copper (Cu, 110 Copper, McMaster) tab having the same size as the polished Al tab acted as the cathode. The two tabs were separated by a 1 cm gap using a 3D printed (TAZ 6, LulzBot) cap. The polished side of the Al anode was placed such that it faced the Cu cathode. The negatively charged SiO₂ particles in the solution were driven to the polished Al plate by an applied voltage generated by a power supply (GW Instek PSW800-1.44) connected between the two tabs. The power supply was set to run with a constant current density of 2.2 mA/cm² during the 10 min deposition process. The voltage was subject to change to maintain the constant current density and was observed to range from ≈10 to ≈200 V. By alteration of the current density and deposition time, different thicknesses of SiO₂ were obtained. A 150 mL PYREX beaker was used in the experiment. The amount of the EPD solution was carefully calculated prior to deposition; hence, the depth of solution was 5 ± 0.1 cm as measured to the bottom of the meniscus. Since the power supply was able to maintain a constant current, and the width of our sample was 2.5 cm, we could ensure that the area immersed in solution was exactly 2.5 cm × 5 cm; hence, we could control the current density. Here, we studied the effect of changing the ratio between the solvent and solute to find an optimum ratio for smooth deposition of SiO₂. Detailed diagrams along with photographs of the EPD process and setup are shown in Figure 1. The final thickness of coating was measured by focused ion beam milling (see Methods section), to be $d_{\text{SiO}_2} \approx 700$ nm.

After completion of the EPD process in the solution, the Al sample was carefully withdrawn from the solution and rinsed gently for 15 s with a 1:1 molar ratio of DI water and ethanol. The sample was then

dried by gently touching the bottom of the sample on an absorbent paper towel to wick away excess solution and allowed to dry at room temperature for 10 min. The Al tab was then sintered in an atmospheric pressure oven (Lindberg/Blue M Moldatherm Box Furnace) at 500 °C for 30 min. The ramp speed was 8 °C/min. Finally, the polished Al sample coated with EPD SiO₂ was then coated with SOCAL using the same procedure developed for the polished Si wafer with double silane concentration (see Silicon Wafer Preparation and SOCAL Coating section).

To obtain a benchmark comparison with the SOCAL coating, we also fabricated highly scalable superhydrophobic Al surfaces using silanization of boehmite. A detailed description of the superhydrophobic Al surface fabrication can be found elsewhere.^{33–37} A second surface, which was smooth and had ultralow contact angle hysteresis, was fabricated for benchmarking antifouling performance. The second surface was a copper-based lubricant infused surface (LIS). A detailed description of the LIS fabrication method used can be found in other literature.^{15,38}

Spin on Glass (SOG). A second method studied for depositing SiO₂ was spin coating. Spin on glass is a well-developed technique used in many applications such as optical waveguide development and lithography.^{39–41} We used a commercial SOG kit (NDG-0500, DesertSilicon). The Al tabs were prepared and cleaned using the same procedure as EPD. The only difference was the size of Al tabs, which for SOG was 2.5 cm × 5 cm × 0.2 cm. The Al tab was placed on a spin coater (Spin 1200T, MIDAS) and coated with the NDG-0500 solution. Since the sample was rectangular in shape, to ensure smooth and full coverage, we put redundant solution on top of the Al tab. The spin coater was programmed to accelerate to 3000 rpm in 10 s, stay at 3000 rpm for 30 s, and decelerate to 0 rpm in 10 s. The thickness of the coating was controlled by the spin speed, with detailed relations provided by DesertSilicon. Here we used 3000 rpm to achieve a 50 nm thick glass coating. After spin coating, the tab was sintered in an atmospheric pressure oven (Lindberg/Blue M Moldatherm Box Furnace) at 600 °C for 30 min. Finally, the polished Al sample coated with SOG SiO₂ was coated with SOCAL using the same procedure developed for the polished Si wafer with double silane concentration.

Sputter Deposition (PVD). Silicon dioxide (SiO₂) sputtering or physical vapor deposition (PVD) was done on a commercial sputter system (AJA Orion 3). Prior to sputtering, the cleaned and dried polished Al tabs were further cut to 2.5 cm × 5 cm × 0.2 cm sizes to ensure full coverage. The Al samples were cleaned using the previously discussed procedure outlined in the EPD section. During sputter deposition, the plasma chamber was first vacuumed to 4 × 10^{−4} Pa, with an argon (Ar) flow rate set to 8.9 mg/min. The RF plasma was initiated at 5 W power. Once the sputter deposition process started, the RF power was increased to 200 W. The estimated deposition rate of SiO₂ was ≈0.1 Å per second. The total deposition time was 25 min; hence, the total thickness of the SiO₂ coating was ≈15 nm. After completion of sputter deposition of SiO₂, the Al samples were coated with SOCAL using the same procedure developed for the polished Si wafer with double silane concentration.

Scanning Electron Microscopy (SEM). SEM images of the fabricated samples (coated and uncoated) were taken with a Hitachi S-4700. Since SiO₂ is nonconductive, a ≈5 nm layer of gold–palladium (Au–Pd) was sputtered on the samples prior to imaging. During imaging, the SEM accelerating voltage was 7 kV, while the emission current was kept at 10 μA. The ultrahigh-resolution viewing mode was used at a working distance of 7 mm. Three images were taken for each sample at 1k, 10k, and 100k magnification. For 1k magnification imaging, spatially random areas in the middle of the samples were chosen. For 10k and 100k magnification imaging, we zoomed in to areas first identified in the 1k magnification imaging and targeted areas of interest, e.g., for EPD samples, areas that showed aggregation of SiO₂ nanoparticles.

Atomic Force Microscopy (AFM). To better quantify the topology and roughness observed with SEM, an Asylum Research Cypher S AFM was used in tapping mode to scan the sample surfaces. Spatially random 5 μm × 5 μm areas were chosen near the center of the samples for scanning. The tip used was a Tap300 (Ted Pella), and the driving

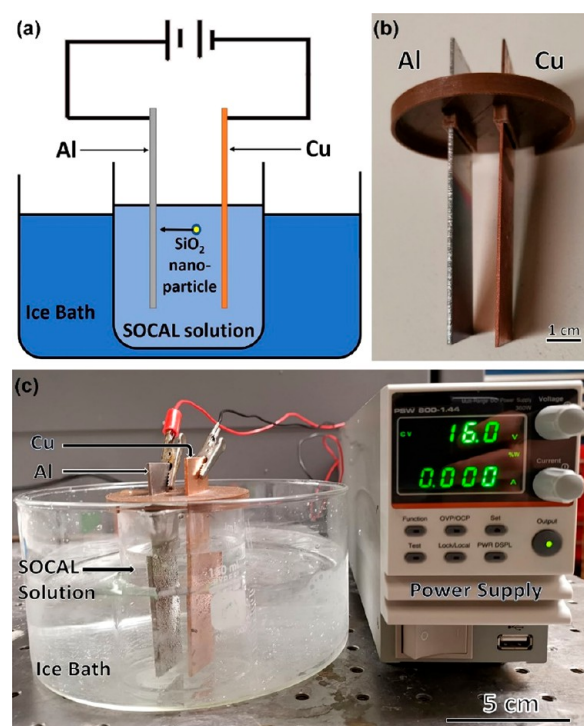


Figure 1. (a) Schematic of EPD setup. SiO₂ particles in solution move to the Al plate due to the generated electric field. (b) Photograph of the 3D printed cap with Al and Cu electrodes inserted. The cap was used to ensure the 1 cm distance between the Cu and Al during EPD. (c) Photograph of the EPD setup. A current density of 2.2 mA/cm² was maintained and the voltage was allowed to change during EPD. The EPD solution volume was calculated for a 2.5 × 5 cm immersed area.

frequency was set to 300 kHz. The scan frequency was 0.5 Hz, with a drive amplitude of ≈ 120 mV. An open source software, Gwyddion,⁴² was used to process the images.

Focused Ion Beam (FIB). To characterize the thickness of coated silicon dioxide layer, we used focused ion beam milling (FIB) (Thermo Scientific Scios DualBeam, FEI Company) and SEM imaging. Milling was performed with normal incidence of the ion beam (sample tilt of 52°), ion beam energy of 30 keV, and ion current of 150 pA. The structure cross sections were obtained by milling $10\ \mu\text{m}$ deep \times $20\ \mu\text{m}$ wide trenches.

Contact Angle Measurement. To characterize the surface chemistry of the SOCAL coated samples, both apparent advancing (ACA) and receding (RCA) contact angles were measured using a microgoniometer (MCA-3, Kyowa Interface Science).^{27,43,44} Samples were placed on a temperature-controlled stage having a chiller feedback loop (AD20R-30-A11B, PolyScience). Two sets of contact angle data were measured, at sample temperatures of 20 ± 2 and 60 ± 5 $^\circ\text{C}$. Samples characterized at higher temperatures were conducted 1 min after placement on the stage to allow for temperature equilibration. The sample surface temperature was measured using an infrared thermometer (Helect) having an uncertainty of ± 2 $^\circ\text{C}$. A piezoelectric dispenser was set 5–10 mm above the sample surface. The dispenser would dispense microscale droplets on the surface, allowing droplets to accumulate into a larger droplet for contact angle characterization. After the water droplet ACA was obtained at 20 $^\circ\text{C}$ sample temperatures with a water droplet dispense rate of 150 Hz, the dispenser was shut off, allowing the water droplet to evaporate and measure the RCA. For tests conducted at 60 $^\circ\text{C}$ sample temperatures, the dispense rate was increased to 300 Hz during ACA measurement since the sessile water droplet evaporated faster. Due to rapid evaporation, the dispenser was kept on during the RCA measurement with a reduced frequency of 50 Hz. All samples were characterized by conducting and averaging the data from at least five independent ACA and RCA measurements on spatially varying locations. All contact angle data were analyzed using the image processing software (FAMAS, interFace Measurement and Analysis System) with the circle fitting method.

Scaling Testing. Scaling was performed in a custom built setup shown in Figure 2. The CaSO_4 solution was made by first pouring 700 mL of DI water in a 1000 mL glass beaker, followed by addition of 0.42 g

of CaSO_4 salt, and vigorous mixing using a PTFE stir bar at 600 rpm for 1 h or until salt is fully dissolved at room temperature. The samples of interest were then immersed in the CaSO_4 aqueous solution (0.06g/100 mL) at a 70° angle relative to the vertical. A custom 3D printed rack (TAZ 6, LulzBot) was used to support each sample. To secure the samples, the back side of the sample was adhered to the rack using double sided tape (3 M Scotch, double sided mounting tape) sized to cover the entire back side of each sample. The beaker was then placed on a hot plate (UX-04600-12, Thermo Scientific) and heated to 65 $^\circ\text{C}$. As the water gradually evaporated from the beaker, CaSO_4 precipitation formed on the sample. To characterize scaling, samples were weighed before and after experiments on a microbalance (AS 82/220.R2, Radwag) having a maximum resolution of 0.01 mg and an uncertainty of ± 0.01 mg. Since the backside of the sample was taped, we observed that scaling only occurred on the front side. This was backed by visual and optical microscopy inspection of samples after removing them carefully from the holder. Since the shape of the Si wafer samples were semicircles, while the Al samples were rectangular, we report the weight added due to scale formation in terms of normalized front facing area, or mg/cm^2 .

To understand the mechanism of scaling from bulk precipitation without the potential presence of liquid–vapor menisci, as well as sample orientation, we conducted a similar scaling test as described above, but with samples laid flat on the bottom of the beaker (coating facing up). In this horizontal configuration, all samples will be covered with precipitation, since all solvent will eventually evaporate. To characterize surface coverage, we obtained photographs of the salt nucleated on the tops of surfaces using both a DSLR camera (SD mark IV, Canon) and optical microscopy (ECLIPSE LV100ND Nikon) with a microscope camera (DS-Qi2, Nikon). Note, Figure 2 does not show the horizontally oriented samples and only depicts the angled sample approach.

Descaling Testing. Descaling was characterized for all samples. We began by synthesizing 500 mL of CaSO_4 aqueous solutions having CaSO_4 concentrations of 0.2 g/100 mL. We studied uncoated Al, glass coated Al, and SOCAL coated Al samples. The glass coated and SOCAL coated Al used the SOG method to create the glass layer. Each coating type had two samples per run to ensure repeatability and consistency. Sample locations were positioned such that flow inhomogeneity could be factored into the analysis of results, with one sample closer to the center of the circular beaker, and the second closer to the edge. Samples were placed at the bottom of the beaker with the coating side facing up, and a PTFE stir bar at the center to control flow conditions. The hot plate was kept at 65 $^\circ\text{C}$ and the stir bar operated at 300 rpm. To make sure all samples would be covered with salt, the water was allowed to completely evaporate from the beaker. After photographs were taken with a DSLR camera (SD mark IV, Canon) of the scaled samples, 300 mL of pure DI water was added into the beaker to initiate descaling. The speed of the stir bar was set to 500 rpm to increase the flow of DI water and to ensure dissolution of the scale product. Photographs were taken in 30 s intervals during stirring.

Thermal Stability Testing. The thermal stability of the SOCAL coatings was tested by heating samples in an atmospheric pressure oven (Lindberg/Blue M Moldatherm Box Furnace) for various time and temperature combinations. After heating, the apparent water droplet advancing and receding contact angles were measured using the microgoniometer. The heating temperature ranged from 150 to 400 $^\circ\text{C}$ and was varied in 50 $^\circ\text{C}$ intervals. At each temperature, five identical samples were placed in the oven. After 1 h, the first sample was taken out, followed by the rest of the samples taken out sequentially at 2, 4, 8, and 16 h. We used change in apparent contact angle as an indicator of coating integrity due to the intrinsic hydrophilicity of the substrate (SiO_2) beneath the SOCAL coating.

Surface Energy Characterization. To characterize the surface energy of the SOCAL coating, we used Lifshitz–van der Waals (LW) interaction theory.^{12,25,45} The total surface energy can be decomposed into three components: γ^{LW} is the Lifshitz–van der Waals component of surface energy, γ^+ and γ^- are the components due to the Lewis acid and Lewis base sites, respectively. The total surface energy can be expressed as

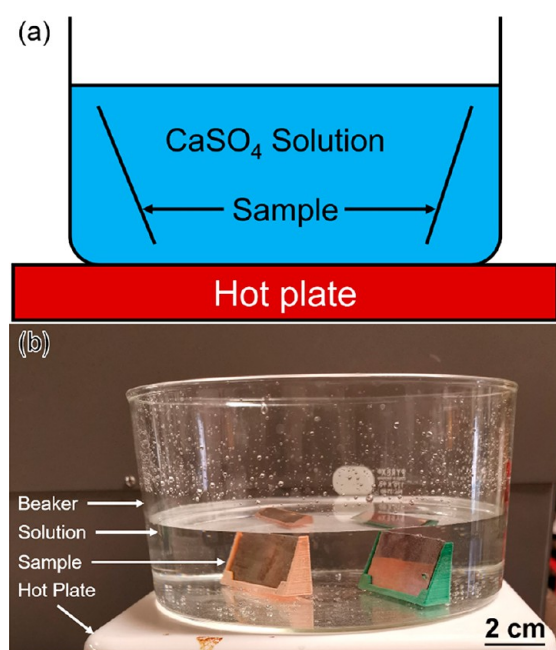


Figure 2. (a) Schematic of the scaling setup. As water gradually evaporates, salt precipitates onto the samples. Schematic not to scale. (b) Picture of the scaling setup showing Cu samples placed on the 3D printed racks.

$$\gamma^{\text{total}} = \gamma^{\text{LW}} + 2\sqrt{\gamma^+ \gamma^-} \quad (1)$$

The contact angle of a certain liquid on a surface can be calculated by

$$\gamma_{li}(1 + \cos \theta_i) = 2(\sqrt{\gamma_s^{\text{LW}} \gamma_{li}^{\text{LW}}} + \sqrt{\gamma_s^+ \gamma_{li}^-} + \sqrt{\gamma_s^- \gamma_{li}^+}) \quad (2)$$

where the subscripts s and l represent solid and liquid and i indicates the liquid used. According to eqs 1 and 2, once γ_{li}^+ , γ_{li}^- , γ_{li}^{LW} as well as the intrinsic equilibrium contact angles are known for three different liquids on a surface of interest, we can determine γ_s^+ , γ_s^- , and γ_s^{LW} of the surface and hence the total surface energy. Here, the equilibrium contact angle is assumed to be an arithmetic mean of the measured ACA and RCA. This was a fair approximation given the ultralow contact angle hysteresis observed for the SOCAL samples (i.e., (ACA – RCA) < 5°).

To determine the surface energy of the SOCAL coating, we used DI water, ethylene glycol (107-21-1, Sigma-Aldrich), and glycerol (56-81-5, Sigma-Aldrich) as the probe liquids. Surface energy data used in the calculation were previously measured experimentally,⁴⁶ with corresponding data used shown in Table 1. Here the ratio between Lewis

Table 1. Total and Individual Surface Energies at Room Temperature and Pressure of DI Water, Diiodomethane, and Toluene and Their Corresponding Contact angles on the SOCAL Coating

probe fluid	γ^{total} [mJ/m ²]	γ^{LW} [mJ/m ²]	γ^+ [mJ/m ²]	γ^- [mJ/m ²]	equilibrium CA
DI water	72.8	21.8	25.5	25.5	104.1 ± 0.6°
ethylene glycol	48	29	1.92	47	88.7 ± 1.1°
glycerol	64	34	3.92	57.4	97.8 ± 1.2°

acid/base components of the surface energy of water is assumed to be 1, while the other probe liquid data were determined according to this ratio. The total surface energy of the SOCAL coating was determined to be $\gamma_{\text{Socal}}^{\text{tot}} = 11.17 \pm 1.51$ mJ/m². The uncertainty stems from propagation of error associated with contact angle characterization using our microgoniometer. A list of surface energies for common materials and other low-surface-energy coatings is shown in Table 2,^{12,47,48} demonstrating the extremely low surface energy of SOCAL, which translates to high antiscaling potential.

Table 2. Surface Energies of Common Metals and Polymers

material	surface energy [mJ/m ²]	ref
Cu	1830	48
Al	1160	48
Fe	2480	48
PDMS	20	47
Kapton(R)	50	47
polyethylene	31	47
uncoated glass	52	12
methylsilane	48	12
dimethylsilane	26	12
SOCAL	11.17 ± 1.51	this work

It is important to note that we also investigated the effect of acid/base components of surface tension on our final result.⁴⁶ The ratio between water acid/base components was assumed to be either 1 or 1.8, as determined from past literature. Hence use of these two components led to different acid/base component in the other probe liquids. Hence no uncertainty in terms of the value was reported since these are assumptions and not experimentally measured values. Furthermore, the ratio between the water acid/base component does not affect the final surface energy appreciably. Indeed, our calculation showed a surface energy of 11.17 mJ/m² when a ratio of 1 was assumed and 11.18 mJ/m² when a ratio of 1.8 was assumed.

■ RESULT AND DISCUSSION

Scaling Theory. To gain an understanding of the effects of surface chemistry and roughness on scaling, we first developed a model based on classical nucleation theory (CNT).^{49,50} The free energy change (ΔG) of a system during heterogeneous nucleation of a spherical nucleus with radius r can be written as

$$\Delta G = \left(-\frac{4}{3}\pi r^3 \Delta g + 4\pi r^2 \sigma_{\text{salt,solution}} \right) f(\theta) \quad (3)$$

where

$$f(\theta) = \frac{2 - 3 \cos \theta + \cos^3 \theta}{4} \quad (4)$$

and

$$\cos \theta = \frac{\sigma_{\text{subs,solution}} - \sigma_{\text{salt,subs}}}{\sigma_{\text{salt,solution}}} \quad (5)$$

The symbol Δg represents the volumetric free energy difference of the nucleating phase, $\sigma_{\text{salt,solution}}$, $\sigma_{\text{salt,subs}}$, and $\sigma_{\text{subs,solution}}$ are the salt–solution, salt–substrate, and substrate–solution interfacial energies, respectively, the salt is the nucleated phase, and $f(\theta)$ is a shape factor accounting for the equilibrium contact angle of the scale on the substrate (θ). Though the salt is soluble in water, when nucleated due to a temperature and solubility change, a salt–solution interface is formed. For simplicity, we assume that (1) the scale nucleus has a spherical cap shape defined by an equilibrium contact angle rather than a polyhedron crystal, and (2) the substrate–salt interfacial energy is well-defined. The theoretical framework shown here is meant to serve as a sensitivity analysis to judge parametric influence on nucleation, rather than accurate nucleation rate predictor. In order to solve for the nucleation rate (J), the critical nucleus radius r^* , must be determined. Differentiating eq 3 with respect to r and setting it to zero, we obtain $r^* = 2\sigma_{\text{salt,solution}}/\Delta g$, with the critical nucleation energy barrier given by

$$\Delta G^* = \frac{16\pi\sigma_{\text{salt,solution}}^3}{3\Delta g^2} f(\theta) \quad (6)$$

Thus, the nucleation rate is

$$J = N_s Z j \exp\left(\frac{-\Delta G^*}{k_B T}\right) \quad (7)$$

where N_s is the number of free nucleation sites on the surface, j is the rate at which molecules attach to the nucleating phase from solution, Z is the Zeldovich factor, representing the probability of a critical nuclei growing into a stable crystal, k_B is the Boltzmann constant, and T is the temperature. Equation 7 reveals that the free parameters available for control during scaling (independent of the working fluid) are the interfacial energy between the substrate and solution ($\sigma_{\text{subs,solution}}$) and the number of free nucleation sites (N_s) on the substrate. For a certain liquid, the lower the surface energy of substrate, the lower the interfacial energy between substrate and liquid. Figure 3 plots J as a function of σ_{subs} for different N_s . The results indicate that to minimize scale nucleation, either the substrate surface energy should be minimized or the number of available nucleation sites should be reduced. The SOCAL coatings used here achieve both goals simultaneously by developing ultralow surface energy, atomically smooth interfaces that are devoid of

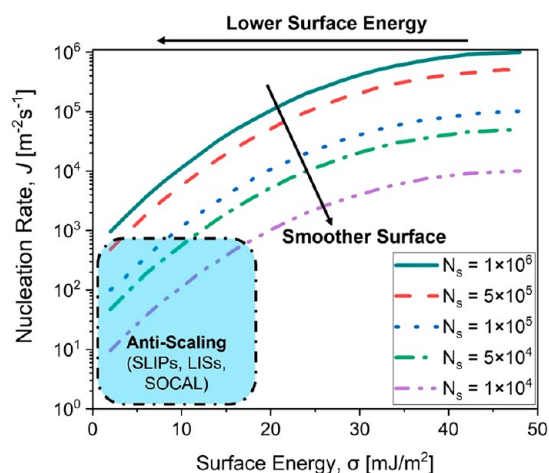


Figure 3. Simulation results showing the heterogeneous nucleation rate (J) of scale on a surface as a function of substrate surface energy (σ) for different nucleation site densities (N_s). As the surface energy reduces and the surface topology becomes smoother, J decreases to the antifouling regime (shaded blue area in the bottom left). The dotted box in the bottom-left corner represents a qualitative region for identifying parameters which will result in reduced scaling or nucleation behavior.

nucleation sites. It is important to note that the plotted curve is for nucleation during heterogeneous water condensation for reasons associated with the values needed for the calculations being readily available. Although qualitative for water condensation, the calculations represent a good qualitative analysis with the argument holding true when switching to slat nucleation.

Surface Roughness. To characterize surface roughness, we first took SEM images for the initial recipe. As observed in Figure

4, the initial recipe (Figure 4a–c) resulted in a rather rough surface, with aggregation of SiO_2 nanoparticles. The aggregation occurred randomly on the surface. In addition to aggregation, we also observed macroscale waviness on the surface due to the uneven distribution of SiO_2 particles. The SiO_2 particles ranged in diameter from 30 to 200 nm. Since many particles assembled onto the surface, the structure peak-to-valley height observed was >200 nm. As mentioned before, the coating should have low-surface-nucleation-site density in order to achieve antiscaling.

With this goal in mind, we changed the recipe of the EPD process to optimize the prepared surface and minimize surface roughness. We varied the ratio between TEOS and MTES during EPD. The original recipe used a base chemical of only TEOS.^{22,24} The result was multiple layers of SiO_2 particles stacking on each other forced onto the Al sample via the electric field. To smooth out the particles, we added MTES to the deposition solution. The difference between TEOS and MTES is that one of the ethoxy groups is replaced by a methyl group. Thus, when gelation occurs, some of the Si–O–Si bonds will break because of the methyl group, resulting in finer control of generated particles. Various samples having differing MTES concentrations over the total silane concentration were fabricated. Each concentration had four samples, with each sample further coated with the SOCAL solution. Three of the samples were coated once, twice, or thrice, while the fourth sample used a double concentration of silane in the SOCAL solution. The contact angle data for these fabricated samples was characterized using the microgoniometer (see Methods), with results listed in Table S1 (see Supporting Information).

The results of different MTES concentrations was verified using SEM images of two sample batches. Parts d–f of Figure 4 show results when the molar ratio of TEOS:MTES was 4:1. Notice that the original paper only used TEOS; here we used

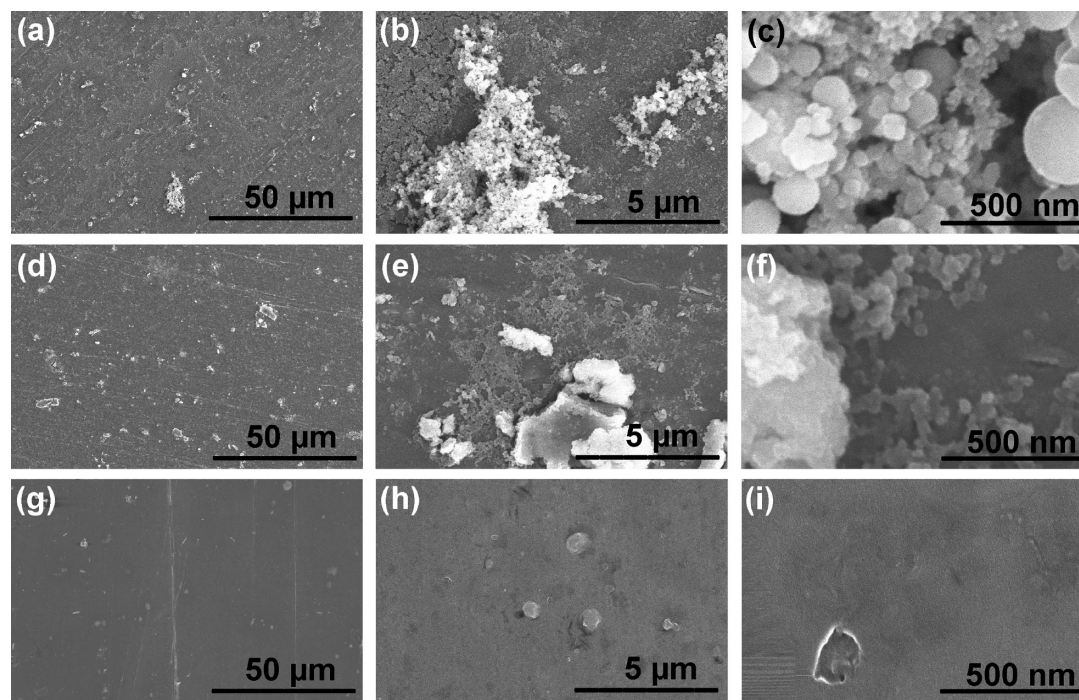


Figure 4. Comparison SEM images of EPD SiO_2 on an Al substrate using (a)–(c) conventional sol–gel, and (d)–(f) modified sol–gel recipes. Utilization of a conventional sol–gel recipe resulted in uneven surfaces with many random aggregations of SiO_2 particles. The modified sol–gel recipe resulted in a smooth surface with reduced roughness.

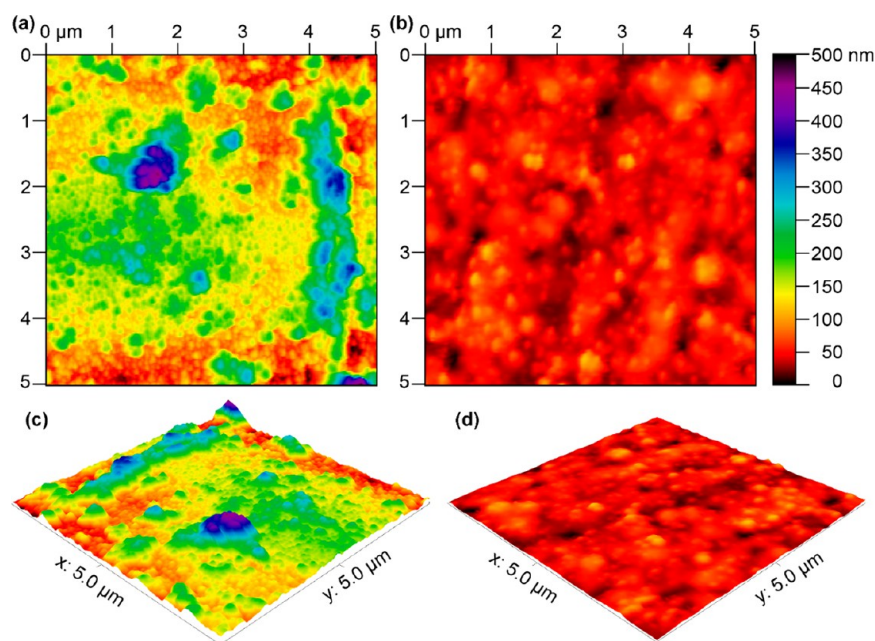


Figure 5. AFM images of EPD SiO₂ on an Al substrate using the (a) conventional sol–gel recipe with SiO₂ particle agglomeration present, and (b) modified sol–gel recipe with agglomeration eliminated. Here (a, b) are 2D top view scans, while (c, d) are 3D topology views. The dimension in the z-axis is proportional to the x- and y-axes. Note that all images share the same color bar, as shown to the right of the image (b).

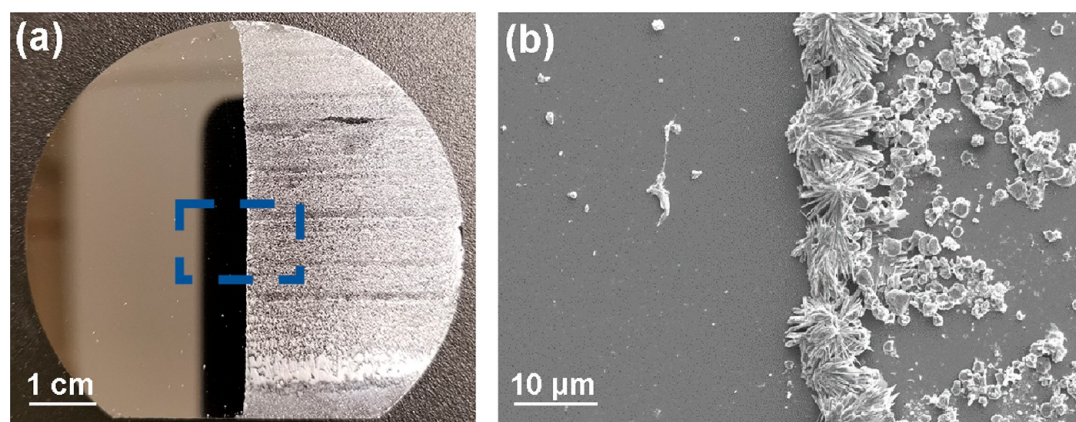


Figure 6. (a) Top-view photograph of the 2 in. polished Si wafer after scaling tests in the angle configuration. The wafer was specially made with the left side coated with SOCAL and right side uncoated (clean SiO₂). A clear vertical line distinguished between the two halves after scaling tests. (b) SEM image of the sample near the center demarked by the blue dashed box in (a). The demarking box in (a) is not to scale.

Table 3. Tilted Sample Scaling Test Results^a

sample name	sample description	ACA [deg]	RCA [deg]	contact angle hysteresis [deg]	wt added (Al sample) (%)	wt added [mg/cm ²]
(a) Si SOCAL	smooth low SE	104.7 ± 0.5	103.5 ± 0.4	1.05 ± 0.6	N/A	0.012
(b) Si uncoated	smooth high SE	43.4 ± 0.4	30.8 ± 0.7	12.6 ± 0.8	N/A	0.190
(c) glass SOCAL	smooth low SE	108.3 ± 0.6	103.9 ± 0.5	4.4 ± 0.8	N/A	0.018
(d) Al uncoated	smooth high SE	7.8 ± 2.6	≈0	7.8 ± 2.6	1.73	0.735
(e) Al EPD SiO ₂ new	smooth low SE	105.5 ± 1.0	102.8 ± 0.6	2.7 ± 1.2	0.09	0.036
(f) Al EPD SiO ₂ old	rough low SE	129.7 ± 0.9	90.4 ± 2.6	39.3 ± 2.8	2.48	0.912
(g) AlPVD SiO ₂	smooth low SE	103.9 ± 1.1	95.4 ± 1.2	8.5 ± 1.6	0.23	0.097
(h) Al HTMS SHP	rough low SE	170.4 ± 1.4	165.4 ± 4.1	5.0 ± 4.3	1.16	0.488
(i) Cu LIS	smooth low SE	121.5 ± 1.7	118.5 ± 2.4	3.0 ± 2.9	N/A	0.028

^aContact angle characterization was conducted with DI water at room temperature. The surface energy is referred to as SE.

some MTES but the concentration was not high enough to eliminate SiO₂ aggregations. In contrast, parts g–i of Figure 4 show the result when we increased the ratio to 1:1. Combining Figure 4d–f and Figure 4g–i, we can see the optimization

process, demonstrating results of the first and latest (optimized) recipe. Surface waviness was eliminated and aggregations appear from single and sporadic defect sites.

To verify the SEM results, we utilized AFM to quantify surface topology with greater resolution. Figure 5a,c shows AFM scans on the unmodified recipe with clear aggregation of SiO₂ particles present, and a peak-to-valley roughness approaching 400 nm. Figure 5b,d shows a much smoother surface, with no aggregations observed, and a reduced roughness of <50 nm.

Scaling Tests. To quantify the antiscaling efficacy of the SOCAL coating, we first conducted scaling tests with a SOCAL coated Si wafer. A special 2 in. diameter Si wafer that is half-coated with SOCAL was manufactured via dip-coating. Microgoniometric measurements (see Methods) of the water contact angle demonstrated ACA/RCA of 104.7°/103.5° on the SOCAL side and 43.4°/30.8° on the uncoated side. The circular sample was placed in an orientation such that the line demarking the two regions was parallel with the gravitational vector. The initial scaling test was conducted with CaSO₄ solution as described in the Methods. The result of the scaling test is shown in Figure 6. Both optical (Figure 6a) and SEM (Figure 6b) images show a clear demarcation separating the coated (left) and uncoated (right) sides, with significantly more CaSO₄ scale buildup on the uncoated side.

After validating the antiscaling properties of SOCAL deposited on SiO₂ wafer substrates, we performed scaling tests on the metal substrates coated with SOCAL using the varying SiO₂ deposition techniques; including SOG, PVD, and EPD (see Methods). Table 3 shows a detailed list of samples used for scaling tests along with their corresponding DI water wettability characterization. The first phenomenon we noticed during experiments was that the hydrophobicity of the sample significantly affected scaling. The salt solution used during testing was not saturated at initiation of the experiment, with the concentration of CaSO₄ being 0.06 g/100 mL. The salt concentration increases as water evaporates from the solution due to heating, eventually reaching the solubility of CaSO₄ dihydrate at 60 °C of 0.244 g/100 mL. Hence, scaling should initiate when the water level reaches approximately 25% of its original volume (i.e., when it reaches saturation) on the tilted samples. However, as observed in Figure 7b,d, scaling occurred on the entire sample for untreated surfaces. Meanwhile, coated samples remained clean to the naked eye even at the very bottom of the sample. Examination of the atomically smooth coated and uncoated Si samples reveals that the difference in scaling behavior can be attributed to the difference in surface energy, as manifested in the ACA/RCA behavior. The Al superhydrophobic (SHP) surface having a rough but low-surface-energy interface resulted in significant scaling. Hence the difference in scaling can be attributed to the difference in surface topology. Only samples having both a smooth surface and low-surface-energy coating showed antiscaling performance (Si SOCAL, Glass SOCAL, EPD SOCAL, PVD SOCAL, or Cu LIS). Note that the SHP sample showed interesting behavior via the inhomogeneous scaling behavior between the top and bottom. The top of the sample was clean, indicating that the surface can prevent scale formation from low-concentration solutions. However, as the concentration of salt increased, more scaling occurred at the bottom of sample, resulting in mediocre antiscaling performance. The Cu LIS sample featured properties similar to those of the SOCAL coating, i.e., low surface energy and smoothness. The main disadvantage of LIS comes from the durability aspects, with studies showing that lubricant drainage over time leads to compromised performance.^{19,20}

Observation of the samples from the front during experiments showed that scaling only occurred at the three-phase contact line

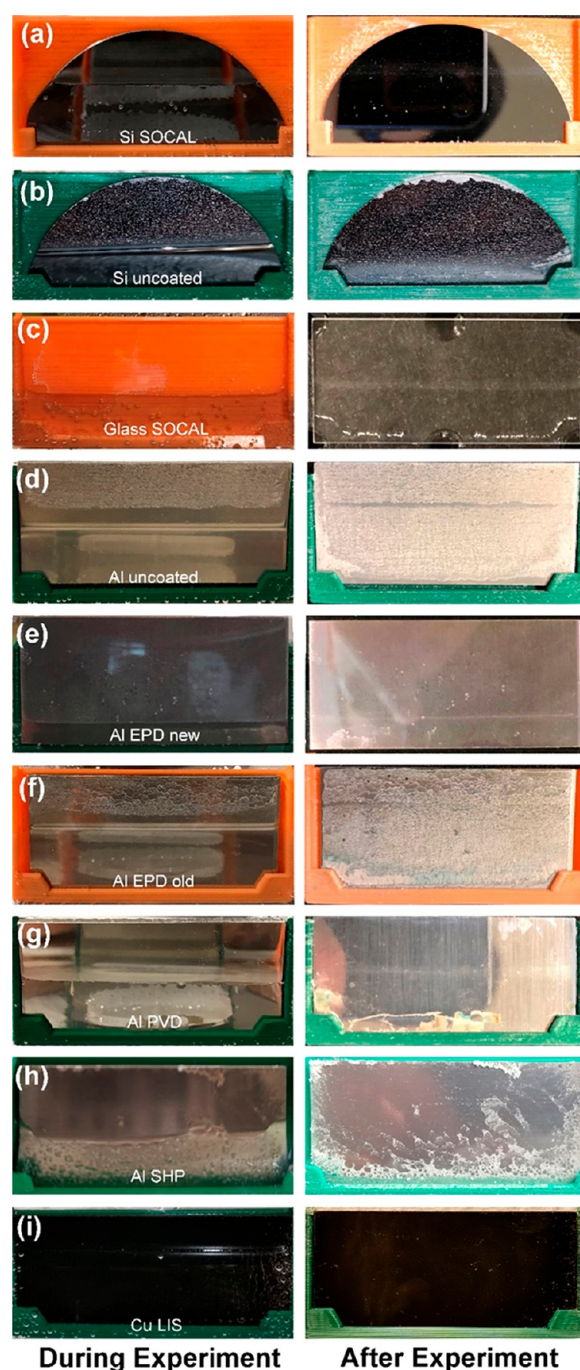


Figure 7. (a)–(i) Tilted-sample static scaling test results on Si SOCAL, Si uncoated, glass SOCAL, Al uncoated, Al EPD new, Al EPD old, Al PVD, Al SHP, and Cu LIS samples, respectively. The left column shows photographs of samples during experiments with the solution meniscus present on the sample (gravity points downward). The right column shows the samples after the experiment is completed and all DI water evaporated. The horizontal dimension of the sample holder and each image is 5 cm.

between the sample surface, liquid salt solution, and vapor. The large contact angle hysteresis and low RCA of hydrophilic surfaces led to the formation of thin films that terminated at the pinned three-phase contact line. The evaporation rate was hence much higher when compared to that for the hydrophobic surfaces, which exhibited high RCA and low hysteresis, with thicker menisci terminating at the mobile contact line. The

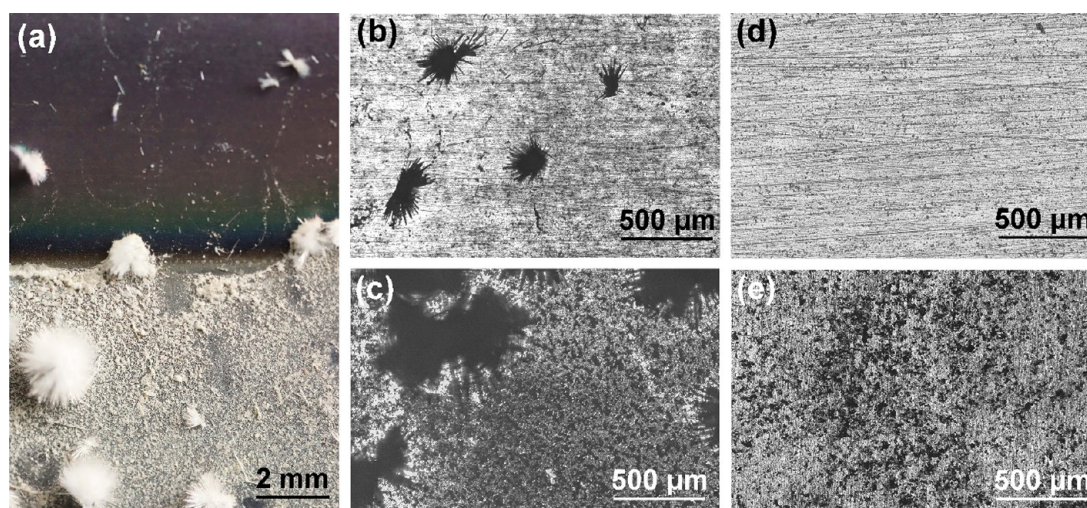


Figure 8. (a) Top-view optical image of an EPD-Al sample made with SOCAL on the top half (dark area) and left bare (uncoated) on the bottom half (scaled area). Top-view optical microscopy images of the (b) SOCAL coated region (top-half in (a)) and (c) uncoated region (bottom-half in (a)). Top-view optical microscopy images of the (d) coated and (e) uncoated samples after vigorously rinsing with DI water from a squeeze bottle.

evaporation-scaling phenomenon can be seen in Figure 7 (left column) with hydrophilic samples showing wetted areas above the solution level (Figure 7b,d). The presence of the extended menisci, and thin film regions led to rapid evaporation,^{51–53} solution resupply and pumping to the contact line, and hence much faster precipitation. This phenomenon has been studied extensively, sometimes termed the “coffee ring effect”.^{54–56} The rapid evaporation-mediated scaling indicates that to minimize scale formation, hydrophobic substrates with minimal contact angle hysteresis are required. Previous studies on the coffee ring effect utilized suspended particulates. The key to the formation of the coffee ring is the pinning of the droplet edge to allow capillary flow to bring particles to the edge.⁵⁶ In our experiment, existing salt crystals at the three-phase interface act as accumulated particles and attract ions to grow on them. Not only does the evaporating interface become supersaturated with the salt ions, but also the porous and wettable scale that forms on the surface acts as a wick, further exacerbating the effect of thin film evaporation and deposition at the contact line.

To mediate the formation of scale due to local supersaturation at the contact line, we utilized the horizontally oriented samples during the scaling test to characterize salt precipitation on completely immersed samples. As described in the Methods section, all samples were placed flat at the bottom of beaker, eliminating the chance of three-phase menisci formation on the samples as water evaporates from the solution. As water evaporated from the solution, a critical supersaturation is reached where all samples will be covered with salt precipitation. However, the pattern of salt formation on the samples is quite different depending on the coating utilized. As shown in Figure 8a, both the pattern and the amount of salt scale dramatically differ on SOCAL coated and uncoated areas of an EPD Al sample. The size of the crystallized salt is much smaller on the SOCAL coated side (top half of Figure 8a), where few amorphous salt particles reside. On the uncoated side (bottom half of Figure 8a), other than the large salt crystal, the surface was covered with amorphous salt precipitation. The differing scale morphology was further verified with optical microscopy, as shown in Figure 8b,c. On the SOCAL coated side (Figure 8b), other than small salt crystals, the bare aluminum substrate can be seen through the EPD coating, whereas the uncoated area

(Figure 8c) is covered with amorphous salt precipitation. In addition to morphology and scale density, the two different types of salt formation vary widely in their adhesion to the substrate. When squeezing a bottle of DI water to wash the dried samples after fouling tests, we found that the large crystallized salt was quite easy to remove, on both the SOCAL coated and uncoated areas. The amorphous salt was much harder to remove. The results of DI water washing are shown in Figure 8 parts d and e, which show optical microscopy images of a scaled area after washing, with stubborn amorphous salt remaining on the uncoated side (Figure 8e).

This descaling experiment shows that the nucleation processes of salt on the coated and uncoated surfaces are fundamentally different. The low-surface-energy coating mitigates nucleation. The amorphous salt evenly covers the uncoated surface, indicating a higher nucleation rate than for the SOCAL coated side. Since the samples were kept flat on the bottom of the scaling solution, prior to all water evaporating, no concentration difference existed across the sample. The results are a clear demonstration of the antiscaling nature of our SOCAL coatings.

Descaling Tests. Descaling of the EPD Al samples via rinsing of DI water from a squeeze bottle (Figure 8) demonstrated qualitatively that the SOCAL coating not only results in reduced scale formation but also limits adhesion of scale when it does occur. To rigorously quantify the descaling performance, additional tests were conducted in a beaker with a more controlled DI water flow field (see Methods). Once room temperature DI water was added to the beaker, descaling occurred in less than 30 s (Figure S1, Supporting Information). Control Al and SOG coated Al (without SOCAL) samples showed minimum change in the amount of salt residing on them after descaling. The descaling results indicate that, in the event of highly supersaturated conditions and scale formation on the SOCAL coated surfaces, the SOCAL samples are easier to clean or descale due to the lower adhesion of salt scale to the interface.

Thermal Stability Testing. Durability testing was done by quantifying coating degradation at elevated temperatures. This was done due to the fact that fouling usually occurs in flow environments that have temperature (and solubility) gradients,⁵⁷ for example, heat exchangers. Furthermore, the wall

shear rate of typical working fluids and flow conditions is not comparable to the shear rate representative of mechanical abrasion. Given that internal piping is typically nonaccessible to human or mechanical contact, thermal stability testing was chosen as the main degradation mode. The SOCAL coating was exposed to different temperature environments for various times. The results of the thermal stability tests are shown in Figure 9. The SOCAL coating started to degrade at a

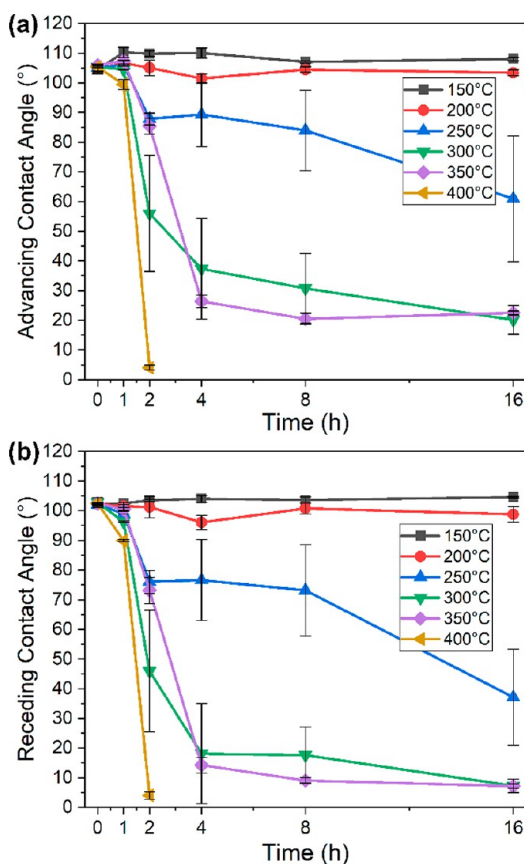


Figure 9. Thermal stability tests for the SOCAL coating demonstrating the (a) apparent advancing contact angle (ACA) and (b) apparent receding contact angle (RCA) of water droplets on the SOCAL surface after various time and temperature exposure in an atmospheric pressure oven. The oven temperature tests ranged from 150 to 400 °C in 50 °C intervals, with times ranging from 1 to 16 h. Tests showed that the SOCAL coating begins to degrade between 200 and 250 °C.

temperature between 200 and 250 °C. Further, more granular tests indicate that the critical temperature was approximately 230 °C. Our results are comparable to those from previous studies on thermal stability of PDMS.⁵⁸ The high degradation temperature shows good potential for our coating in low-temperature applications (such as those using water as the working fluid) showing excellent antifouling behavior at temperatures lower than 100 °C. Although the 230 °C limitation may be beneficial for accretion mitigation at elevated temperatures (hydrocarbon coking),^{59,60} additional studies are needed to prove the efficacy of our approach at elevated temperatures.

DISCUSSION

An interesting aspect about the need for depositing SiO₂ or glass as an intermediary layer for SOCAL bonding is the obvious implications to corrosion prevention. Indeed, EPD of SiO₂ has

widely been studied as a method for creating corrosion barriers on metallic substrates.^{61,62} Hence, the addition of the intermediate EPD SiO₂ layer not only acts to enable antiscaling functionality but also protects the substrate from corrosion depending on the electrochemistry of the flow. Although similar studies of utilizing lubricant-based SLIPS and LIS exist, showing good anticorrosion behavior,^{63,64} these studies mainly utilize methods such as electrochemical impedance spectroscopy to quantify corrosion behavior. Impedance spectroscopy, although accurate and quantifiable, does not mimic the real life scenarios. Depend on the environment, shear forces from flow, diffusion of lubricant, and other loss mechanisms^{19,20} impact corrosion performance. The coating developed here is solid state, has similar or better anticorrosion performance with lubricant-based approaches, and is more durable due to the elimination of lubricant drainage.

One of the main applications where scaling is encountered is in heat transfer equipment.^{65–67} Thermal systems such as boilers, steam generators, and evaporators can encounter significant fouling due to scale formation near regions of phase transition and high supersaturation. The requirement of an amorphous SiO₂ intermediate layer requires analysis of the effect of the EPD SOCAL coating on overall thermal performance due to the added parasitic thermal resistance of the SiO₂ layer. We estimate that the amorphous SiO₂ layer will have an intrinsic thermal conductivity approaching that of glass, or $\approx 1 \text{ W/(m}\cdot\text{K)}$, far less than aluminum ($k_{\text{Al}} = 205 \text{ W/(m}\cdot\text{K)}$). Assuming both sides of a 2 mm thick aluminum wall (d_{Al}) are not coated, with forced single-phase liquid convection with a heat transfer coefficient of h , the overall conductance (U) becomes

$$\frac{1}{U} = \frac{2}{h} + \frac{d_{\text{Al}}}{k_{\text{Al}}} \quad (8)$$

Now, adding two layers of EPD SiO₂ into the equation and assuming negligible thermal resistance due to the SOCAL coating owing to its nanoscale thickness, the overall conductance (U_{coated}) becomes^{68,69}

$$\frac{1}{U_{\text{coated}}} = 2 \left(\frac{1}{h} + \frac{d_{\text{SiO}_2}}{k_{\text{SiO}_2}} \right) + \frac{d_{\text{Al}}}{k_{\text{Al}}} \quad (9)$$

Taking the ratio of eq 8 and 9 reveals that the conductance ratio is

$$\frac{U - U_{\text{coated}}}{U} = \left(1 + \frac{k_{\text{SiO}_2}(2k_{\text{Al}} + hd_{\text{Al}})}{2hd_{\text{SiO}_2}k_{\text{Al}}} \right)^{-1} \quad (10)$$

Figure 10 shows the conductance ratio as a function of SiO₂ thickness (d_{SiO_2}) for a variety of h representative of both one- and two-phase flows. For realistic conditions, assuming $d_{\text{SiO}_2} = 700 \text{ nm}$ (indicative of the coatings developed here using EPD), this thickness is measured by FIB (see Methods section); results of FIB can be found in the Supporting Information (Figure S3). Convective heat transfer coefficients (HTCs) $h = 3 \text{ kW/(m}^2\cdot\text{K)}$ for a single-phase turbulent water flow, $U_{\text{coated}}/U \approx 0.998$, or a 0.2% reduction in overall conductance. Given our ability to tailor the thickness of the SiO₂ layer, the analysis indicates that the thermal implications of the antifouling coatings developed here are negligible and well worth the benefit of added scale-reduction, which created longer term efficient heat transfer performance as well as reduced pressure drop and energy utilization.

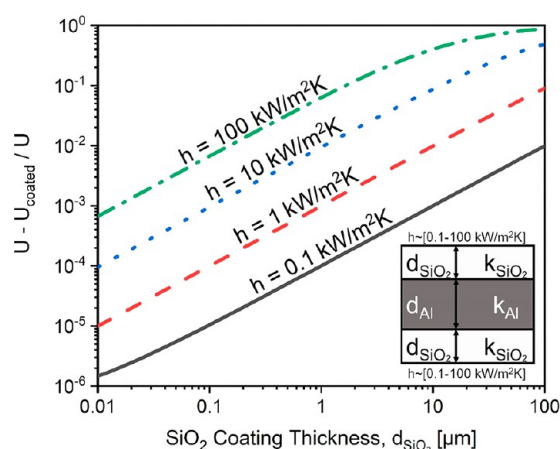


Figure 10. Percent decrease in the overall heat transfer coefficient (U) of an uncoated bare Al surface in comparison to that for a SOCAL coated Al surface (U_{coated}) as a function of coating thickness for a variety of fluid-side heat transfer coefficients (h) on both sides of the Al wall. Only for $h = 100 \text{ kW}/(\text{m}^2\cdot\text{K})$ does the SiO_2 coating have an impact ($>10\%$) on the overall conductance. The thermal conductivity and thickness of the metal wall material are assumed to be $d_{\text{Al}} = 205 \text{ W}/(\text{m}\cdot\text{K})$ and $d_{\text{Al}} = 2 \text{ mm}$, respectively.

The initial study that developed the SOCAL approach demonstrated good thermal stability and durability.²¹ Specifically, the wetting behavior had negligible change one year after manufacture. A negligible change in wetting was observed after 1000 h of exposure in a 100°C ambient environment. Durability of any coating is key to long-term utilization as it implies less maintenance required after deployment. We have further explored the thermal stability of SOCAL. However, our tests were limited to air environments. Interaction between water and soluble salts at elevated temperatures with SOCAL are unknown. Significant work is needed to prove the concept at elevated temperatures and aggressive utilization scenarios.

The use of superhydrophobic surfaces has been a topic of significant interest for the creation of antiscaling coatings. Superhydrophobicity relies on maintenance of the Cassie–Baxter state. Transition from the Cassie–Baxter to the Wenzel state due to elevated hydraulic pressure results in significant changes in wetting and antiscaling behavior.^{70,71} The significant risk of coating failure due to Wenzel transition, from pressure of phase-change within structures, indicates that the use of superhydrophobicity may result in early failure. Once the salt-solution penetrates the structures on a superhydrophobic surface, these structures will act as the nucleation sites for salt crystals and may result in increased adhesion, higher scaling rates, and early failure when compared to results for uncoated surfaces. Indeed, we used a superhydrophobic Al reference sample in our test results, showing worse performance than the ultrasoother EPD SOCAL coating. The ability to create smooth surfaces devoid of any porosity and structure, such as shown here, enables reduced failure modes.

Our scaling tests show that antiscaling is achieved by modifying both surface chemistry and roughness. However, analogous to filmwise-to-dropwise condensation transition,⁷² a critical value for roughness and surface energy to determine when antiscaling performance is enacted is unclear. Due to the complexity of the interaction between roughness and surface chemistry (difficult to decouple the two), the contact angle hysteresis (CAH) is considered as a measure of the “goodness” of a surface. A rough surface (old EPD sample), even with the

SOCAL chemistry yielded high CAH ($\approx 40^\circ$). The new EPD sample with roughness $<50 \text{ nm}$ reduced the CAH ($\approx 3^\circ$). Overall, we estimate that $\text{CAH} < 5^\circ$ represents a good guideline for preparing high-quality SOCAL coatings.

In addition to salt scaling, the developed SOCAL coating methodology has many other antifouling applications where elevated temperatures and nonaqueous working fluids dominate. For example, jet fuel fouling or coking is a significant problem encountered in the aviation and petrochemical industries.^{59,73} Kerosene, when under thermal stress, will decompose and create deposits on wetted materials. This phenomenon causes many problems in aviation applications given the use of jet fuel as an avionics coolant. Previous approaches to mitigate jet fuel deposition and breakdown include limiting the maximum wetted wall temperature and including additives to the fuel (cite). Limiting the maximum wetted wall temperature reduces overall aviation heat exchanger performance, requiring a larger area and size to overcome the barriers. The coating developed here has the potential to migrate fuel deposition with potential of collection of deposits downstream due to the reduced adhesion to the material of interest.

Although demonstrated here for Al substrates, the coating methodology needs to be extended to other materials having varying electrochemical activity. In the future, additional work is needed to explore other metal substrates such as copper (HVAC&R), stainless steel (food processing), titanium (naval), or nickel superalloy (aviation) substrates. Development of a universal coating methodology that can be applied on arbitrary surfaces has the potential to add significant value to industrial applications. Cost estimates based on the coating methodology developed here result in a coating cost of $\$1.5/\text{m}^2$, requiring additional investigation of future supply chain integration with existing products. In addition to scale-up, future work is required to test the antiscaling and anticorrosion efficacy of our coatings in flow conditions with significant shear effects, as well as relevant corrosion conditions used to emulate accelerated lifetime testing conditions such as the ASTM G85 A3 (SWAAT) test in a commercial corrosion tester.

CONCLUSIONS

In conclusion, we have achieved a solid state antiscaling coating on an aluminum substrate by combining SiO_2 coating and SOCAL coating. The SiO_2 coating can have various application techniques, PVD, SOP, or EPD. This coating has great potential in industry for antiscaling. The idea behind this is a low-surface-energy coating and smooth surface topology. We have calculated the surface energy of the SOCAL coating using Lifshitz theory and verified the SiO_2 coating is indeed smooth by both SEM and AFM. With our customized scaling test, the coated sample shows up to $20\times$ less salt scaling than the uncoated sample. In the scaling test, we verified both surface energy and surface smoothness play an important role in scaling. The samples with smooth surfaces and SOCAL coating all show good results. The sample with rough EPD coating and SOCAL (low surface energy) shows scaling after the experiment, and the smooth Si wafer without SOCAL coating also shows scaling after the experiment. This means both factors are important in antiscaling. To demonstrate the antiscaling test we did was not simply the “coffee ring effect”, we forced scaling onto samples by putting them at the bottom of the beaker. The patterns of amorphous salt on coated and uncoated sides show evidence of a difference in mechanism while salt nucleates on

them. We also verified the intermediate layer SiO_2 with various application techniques all works fine in terms of antiscaling. PVD and SOG are limited to size and surface curvature. EPD is a more versatile method to apply SiO_2 . In the descaling test, the SOCAL coating again shows great performance. Low surface energy means salt can be easily removed after scaling. Overall, SOCAL combined with an intermediate layer of SiO_2 could have great potential in antiscaling and we plan to further verify it in future studies.

■ ASSOCIATED CONTENT

SI Supporting Information

The Supporting Information is available free of charge at <https://pubs.acs.org/doi/10.1021/acsami.9b22145>.

Descaling photographs, FIB results, contact angle data for various EPD recipes (PDF)

■ AUTHOR INFORMATION

Corresponding Author

Nenad Miljkovic – Department of Mechanical Science and Engineering and Department of Electrical and Computer Engineering, University of Illinois at Urbana—Champaign, Urbana, Illinois 61801, United States; Materials Research Laboratory, University of Illinois, Urbana, Illinois 61801, United States; International Institute for Carbon Neutral Energy Research (WPI-I2CNER), Kyushu University, Fukuoka 819-0395, Japan; orcid.org/0000-0002-0866-3680; Email: nmiljkov@illinois.edu

Authors

Hanyang Zhao – Department of Mechanical Science and Engineering, University of Illinois at Urbana—Champaign, Urbana, Illinois 61801, United States; orcid.org/0000-0003-0949-381X

Chirag Anand Deshpande – Department of Mechanical Science and Engineering, University of Illinois at Urbana—Champaign, Urbana, Illinois 61801, United States

Longnan Li – Department of Mechanical Science and Engineering, University of Illinois at Urbana—Champaign, Urbana, Illinois 61801, United States; orcid.org/0000-0003-0225-3303

Xiao Yan – Department of Mechanical Science and Engineering, University of Illinois at Urbana—Champaign, Urbana, Illinois 61801, United States; orcid.org/0000-0001-9948-3468

Muhammad Jahidul Hoque – Department of Mechanical Science and Engineering, University of Illinois at Urbana—Champaign, Urbana, Illinois 61801, United States; orcid.org/0000-0002-8036-4511

Gowtham Kuntumalla – Department of Mechanical Science and Engineering, University of Illinois at Urbana—Champaign, Urbana, Illinois 61801, United States; orcid.org/0000-0002-4976-4939

Manjunath C Rajagopal – Department of Mechanical Science and Engineering, University of Illinois at Urbana—Champaign, Urbana, Illinois 61801, United States; orcid.org/0000-0001-7230-2946

Ho Chan Chang – Department of Mechanical Science and Engineering, University of Illinois at Urbana—Champaign, Urbana, Illinois 61801, United States; orcid.org/0000-0002-6604-0772

Yuquan Meng – Department of Mechanical Science and Engineering, University of Illinois at Urbana—Champaign,

Urbana, Illinois 61801, United States; orcid.org/0000-0002-4818-5185

Sreenath Sundar – Department of Mechanical Science and Engineering, University of Illinois at Urbana—Champaign, Urbana, Illinois 61801, United States

Placid Ferreira – Department of Mechanical Science and Engineering, University of Illinois at Urbana—Champaign, Urbana, Illinois 61801, United States

Chenhui Shao – Department of Mechanical Science and Engineering, University of Illinois at Urbana—Champaign, Urbana, Illinois 61801, United States; orcid.org/0000-0002-3299-2222

Srinivasa Salapaka – Department of Mechanical Science and Engineering, University of Illinois at Urbana—Champaign, Urbana, Illinois 61801, United States

Sanjiv Sinha – Department of Mechanical Science and Engineering, University of Illinois at Urbana—Champaign, Urbana, Illinois 61801, United States

Complete contact information is available at: <https://pubs.acs.org/doi/10.1021/acsami.9b22145>

Notes

The authors declare no competing financial interest.

■ ACKNOWLEDGMENTS

We acknowledge support from the Advanced Manufacturing Office (AMO) of the Office of Energy Efficiency and Renewable Energy (EERE) under the U.S. Department of Energy, through the grant DE-EE0008312. The authors gratefully acknowledge funding support from the Air Conditioning and Refrigeration Center (ACRC), an NSF founded I/UCRC at UIUC. N.M. gratefully acknowledges funding support from the International Institute for Carbon Neutral Energy Research (WPI-I2CNER), sponsored by the Japanese Ministry of Education, Culture, Sports, Science and Technology. Scanning electron microscopy, atomic force microscopy and focused ion beam milling was carried out in part in the Materials Research Laboratory Central Facilities, University of Illinois.

■ REFERENCES

- (1) Fritzmann, C.; Löwenberg, J.; Wintgens, T.; Melin, T. State-of-the-Art of Reverse Osmosis Desalination. *Desalination* **2007**, 216 (1–3), 1–76.
- (2) Gill, J. S. A Novel Inhibitor for Scale Control in Water Desalination. *Desalination* **1999**, 124 (1–3), 43–50.
- (3) Müller-Steinhagen, H.; Malayeri, M. R.; Watkinson, A. P. Fouling of Heat Exchangers-New Approaches to Solve an Old Problem. *Heat Transfer Eng.* **2005**, 26 (1), 1–4.
- (4) Vazirian, M. M.; Charpentier, T. V.; de Oliveira Penna, M.; Neville, A. Surface Inorganic Scale Formation in Oil and Gas Industry: As Adhesion and Deposition Processes. *J. Pet. Sci. Eng.* **2016**, 137, 22–32.
- (5) Awais, M.; Bhuiyan, A. A. Recent Advancements in Impedance of Fouling Resistance and Particulate Depositions in Heat Exchangers. *Int. J. Heat Mass Transfer* **2019**, 141, 580–603.
- (6) Steinhagen, R.; Müller-Steinhagen, H.; Maani, K. Problems and Costs Due to Heat Exchanger Fouling in New Zealand Industries. *Heat Transfer Eng.* **1993**, 14 (1), 19–30.
- (7) Zhan, F.; Tang, J.; Ding, G.; Zhuang, D. Experimental Investigation on Particle Deposition Characteristics of Wavy Fin-and-Tube Heat Exchangers. *Appl. Therm. Eng.* **2016**, 99, 1039–1047.
- (8) Gudmundsson, O.; Palsson, O. P.; Palsson, H.; Lalot, S. Online Fouling Detection of Domestic Hot Water Heat Exchangers. *Heat Transfer Eng.* **2016**, 37 (15), 1231–1241.

- (9) Kho, T.; Zettler, H.; Müller-Steinhagen, H.; Hughes, D. Effect of Flow Distribution on Scale Formation in Plate and Frame Heat Exchangers. *Chem. Eng. Res. Des.* **1997**, *75* (7), 635–640.
- (10) Förster, M.; Bohnet, M. Modification of Molecular Interactions at the Interface Crystal/Heat Transfer Surface to Minimize Heat Exchanger Fouling. *Int. J. Therm. Sci.* **2000**, *39* (7), 697–708.
- (11) Subramanyam, S. B.; Azimi, G.; Varanasi, K. K. Designing Lubricant-Impregnated Textured Surfaces to Resist Scale Formation. *Adv. Mater. Interfaces* **2014**, *1* (2), 1300068.
- (12) Azimi, G.; Cui, Y.; Sabanska, A.; Varanasi, K. K. Scale-Resistant Surfaces: Fundamental Studies of the Effect of Surface Energy on Reducing Scale Formation. *Appl. Surf. Sci.* **2014**, *313*, 591–599.
- (13) Masoudi, A.; Irajizad, P.; Farokhnia, N.; Kashyap, V.; Ghasemi, H. Antiscaling Magnetic Slippery Surfaces. *ACS Appl. Mater. Interfaces* **2017**, *9* (24), 21025–21033.
- (14) Kashchiev, D. *Nucleation*; Elsevier, 2000.
- (15) Wong, T.-S.; Kang, S. H.; Tang, S. K. Y.; Smythe, E. J.; Hatton, B. D.; Grinthal, A.; Aizenberg, J. Bioinspired Self-Repairing Slippery Surfaces with Pressure-Stable Omniphobicity. *Nature* **2011**, *477* (7365), 443–447.
- (16) Anand, S.; Paxson, A. T.; Dhiman, R.; Smith, J. D.; Varanasi, K. K. Enhanced Condensation on Lubricant-Impregnated Nanotextured Surfaces. *ACS Nano* **2012**, *6* (11), 10122–10129.
- (17) Lafuma, A.; Quéré, D. Slippery Pre-Suffused Surfaces. *EPL* **2011**, *96* (5), 56001.
- (18) Wang, N.; Xiong, D.; Pan, S.; Wang, K.; Shi, Y.; Deng, Y. Robust Superhydrophobic Coating and the Anti-Icing Properties of Its Lubricants-Infused-Composite Surface under Condensing Condition. *New J. Chem.* **2017**, *41* (4), 1846–1853.
- (19) Liu, Y.; Wexler, J. S.; Stone, H. A.; Schönecker, C. Effect of Viscosity Ratio on the Shear-Driven Failure of Liquid-Infused Surfaces. *Physical Review Fluids* **2016**, *1* (7), 074003.
- (20) Kreder, M. J.; Daniel, D.; Lemaire, B.; Timonen, J. V. I.; Aizenberg, J.; Tetreault, A.; Cao, Z. Film Dynamics and Lubricant Depletion by Droplets Moving on Lubricated Surfaces. *Phys. Rev. X* **2018**, *8* (3), 031053.
- (21) Wang, L.; McCarthy, T. J. Covalently Attached Liquids: Instant Omniphobic Surfaces with Unprecedented Repellency. *Angew. Chem., Int. Ed.* **2016**, *55* (1), 244–248.
- (22) Kishida, K.; Tatsumisago, M.; Minami, T. Preparation of Thick Silica Films by Combined Sol-Gel and Electrophoretic Deposition Methods. *Nippon Seramikkusu Kyokai Gakujutsu Ronbunshi* **1994**, *102*, 336–340.
- (23) Castro, Y.; Ferrari, B.; Moreno, R.; Durán, A. Corrosion Behaviour of Silica Hybrid Coatings Produced from Basic Catalysed Particulate Sols by Dipping and Epd. *Surf. Coat. Technol.* **2005**, *191* (2), 228–235.
- (24) Nishimori, H.; Tatsumisago, M.; Minami, T. Preparation of Thick Silica Films by the Electrophoretic Sol-Gel Deposition on a Stainless Steel Sheet. *Nippon Seramikkusu Kyokai Gakujutsu Ronbunshi* **1995**, *103* (1193), 78–80.
- (25) Van Oss, C. J.; Chaudhury, M. K.; Good, R. J. Interfacial Lifshitz-Van Der Waals and Polar Interactions in Macroscopic Systems. *Chem. Rev.* **1988**, *88* (6), 927–941.
- (26) Preston, D. J.; Miljkovic, N.; Sack, J.; Enright, R.; Queeney, J.; Wang, E. N. Effect of Hydrocarbon Adsorption on the Wettability of Rare Earth Oxide Ceramics. *Appl. Phys. Lett.* **2014**, No. 1, 011601.
- (27) Yan, X.; Huang, Z.; Sett, S.; Oh, J.; Cha, H.; Li, L.; Feng, L.; Wu, Y.; Zhao, C.; Orejon, D.; Chen, F.; Miljkovic, N. Atmosphere-Mediated Superhydrophobicity of Rationally Designed Micro/Nanostructured Surfaces. *ACS Nano* **2019**, *13* (4), 4160–4173.
- (28) Arkles, B. *Hydrophobicity, Hydrophilicity and Silane Surface Modification*; Gelest Inc.: Morrisville, 2011.
- (29) Zhuravlev, L. T. Concentration of Hydroxyl Groups on the Surface of Amorphous Silicas. *Langmuir* **1987**, *3* (3), 316–318.
- (30) Tamura, H.; Tanaka, A.; Mita, K.-y.; Furuichi, R. Surface Hydroxyl Site Densities on Metal Oxides as a Measure for the Ion-Exchange Capacity. *J. Colloid Interface Sci.* **1999**, *209* (1), 225–231.
- (31) Hoyas, A. M.; Whelan, C.; Schuhmacher, J.; Celis, J.; Maex, K. Effect of Surface Reactive Site Density and Reactivity on the Growth of Atomic Layer Deposited Wn X C Y Films. *Electrochem. Solid-State Lett.* **2006**, *9* (7), F64–F68.
- (32) Poli, E.; Ouk, T.-S.; Barrière, G.; Lévêque, G.; Sol, V.; Denes, E. Does Low Hydroxyl Group Surface Density Explain Less Bacterial Adhesion on Porous Alumina? *Orthopaedics & Traumatology: Surgery & Research* **2019**, *105* (3), 473–477.
- (33) Weisensee, P. B.; Wang, Y.; Qian, H.; Schultz, D.; King, W. P.; Miljkovic, N. Condensate Droplet Size Distribution on Lubricant-Infused Surfaces. *Int. J. Heat Mass Transfer* **2017**, *109*, 187–199.
- (34) Chavan, S.; Park, D.; Singla, N.; Sokalski, P.; Boyina, K.; Miljkovic, N. Effect of Latent Heat Released by Freezing Droplets During Frost Wave Propagation. *Langmuir* **2018**, *34* (22), 6636–6644.
- (35) Boyina, K. S.; Mahvi, A. J.; Chavan, S.; Park, D.; Kumar, K.; Lira, M.; Yu, Y.; Gunay, A. A.; Wang, X.; Miljkovic, N. Condensation Frosting on Meter-Scale Superhydrophobic and Superhydrophilic Heat Exchangers. *Int. J. Heat Mass Transfer* **2019**, *145*, 118694.
- (36) Reed, J. H.; Gonsalves, A. E.; Román, J. K.; Oh, J.; Cha, H.; Dana, C. E.; Toc, M.; Hong, S.; Hoffman, J. B.; Andrade, J. E.; Jo, K. D.; Alleyne, M.; Miljkovic, N.; Cropek, D. M. Ultrascalable Multifunctional Nanoengineered Copper and Aluminum for Antiadhesion and Bactericidal Applications. *ACS Applied Bio Materials* **2019**, *2* (7), 2726–2737.
- (37) Jafari, R.; Farzaneh, M. Fabrication of Superhydrophobic Nanostructured Surface on Aluminum Alloy. *Appl. Phys. A: Mater. Sci. Process.* **2011**, *102* (1), 195–199.
- (38) Sett, S.; Sokalski, P.; Boyina, K.; Li, L.; Rabbi, K. F.; Auby, H.; Foulkes, T.; Mahvi, A.; Barac, G.; Bolton, L. W.; Miljkovic, N. Stable Dropwise Condensation of Ethanol and Hexane on Rationally Designed Ultrascalable Nanostructured Lubricant-Infused Surfaces. *Nano Lett.* **2019**, *19* (8), 5287–5296.
- (39) Holmes, A. S.; Syms, R. R. A.; Li, M.; Green, M. Fabrication of Buried Channel Waveguides on Silicon Substrates Using Spin-on Glass. *Appl. Opt.* **1993**, *32* (25), 4916–4921.
- (40) Kohl, A. T.; Mimna, R.; Shick, R.; Rhodes, L.; Wang, Z. L.; Kohl, P. A. Low K, Porous Methyl Silsesquioxane and Spin-on-Glass. *Electrochem. Solid-State Lett.* **1999**, *2* (2), 77–79.
- (41) Matsui, S.; Igaku, Y.; Ishigaki, H.; Fujita, J.; Ishida, M.; Ochiai, Y.; Komuro, M.; Hiroshima, H. Room Temperature Replication in Spin on Glass by Nanoimprint Technology. *J. Vac. Sci. Technol., B: Microelectron. Process. Phenom.* **2001**, *19* (6), 2801–2805.
- (42) Nečas, D.; Klapetek, P. Gwyddion: An Open-Source Software for Spm Data Analysis. *Central European Journal of Physics* **2012**, *10* (1), 181–188.
- (43) Yan, X.; Zhang, L.; Sett, S.; Feng, L.; Zhao, C.; Huang, Z.; Vahabi, H.; Kota, A. K.; Chen, F.; Miljkovic, N. Droplet Jumping: Effects of Droplet Size, Surface Structure, Pinning, and Liquid Properties. *ACS Nano* **2019**, *13* (2), 1309–1323.
- (44) Günay, A. A.; Sett, S.; Oh, J.; Miljkovic, N. Steady Method for the Analysis of Evaporation Dynamics. *Langmuir* **2017**, *33* (43), 12007–12015.
- (45) Bargir, S.; Dunn, S.; Jefferson, B.; Macadam, J.; Parsons, S. The Use of Contact Angle Measurements to Estimate the Adhesion Propensity of Calcium Carbonate to Solid Substrates in Water. *Appl. Surf. Sci.* **2009**, *255* (9), 4873–4879.
- (46) Lee, L.-H. Correlation between Lewis Acid-Base Surface Interaction Components and Linear Solvation Energy Relationship Solvatochromic A and B Parameters. *Langmuir* **1996**, *12* (6), 1681–1687.
- (47) Dillard, D. A. *Advances in Structural Adhesive Bonding*; Elsevier Inc., 2010; pp 1–637.
- (48) Aqra, F.; Ayyad, A. Surface Energies of Metals in Both Liquid and Solid States. *Appl. Surf. Sci.* **2011**, *257*, 6372.
- (49) Karthika, S.; Radhakrishnan, T. K.; Kalaichelvi, P. A Review of Classical and Nonclassical Nucleation Theories. *Cryst. Growth Des.* **2016**, *16* (11), 6663–6681.

- (50) Sear, R. P. Nucleation: Theory and Applications to Protein Solutions and Colloidal Suspensions. *J. Phys.: Condens. Matter* **2007**, *19* (3), 033101.
- (51) Maroo, S. C.; Chung, J. Heat Transfer Characteristics and Pressure Variation in a Nanoscale Evaporating Meniscus. *Int. J. Heat Mass Transfer* **2010**, *53* (15–16), 3335–3345.
- (52) Xiao, R.; Maroo, S. C.; Wang, E. N. Negative Pressures in Nanoporous Membranes for Thin Film Evaporation. *Appl. Phys. Lett.* **2013**, *102* (12), 123103.
- (53) Plawsky, J.; Fedorov, A.; Garimella, S.; Ma, H.; Maroo, S. C.; Chen, L.; Nam, Y. Nano- and Microstructures for Thin-Film Evaporation—a Review. *Nanoscale Microscale Thermophys. Eng.* **2014**, *18* (3), 251–269.
- (54) Denkov, N. D.; Velev, O.; Kralchevsky, P.; Ivanov, I.; Yoshimura, H.; Nagayama, K. Two-Dimensional Crystallization. *Nature* **1993**, *361* (6407), 26.
- (55) Deegan, R. D.; Bakajin, O.; Dupont, T. F.; Huber, G.; Nagel, S. R.; Witten, T. A. Capillary Flow as the Cause of Ring Stains from Dried Liquid Drops. *Nature* **1997**, *389* (6653), 827.
- (56) Yunker, P. J.; Still, T.; Lohr, M. A.; Yodh, A. G. Suppression of the Coffee-Ring Effect by Shape-Dependent Capillary Interactions. *Nature* **2011**, *476* (7360), 308–311.
- (57) Panchal, C. B.; Knudsen, J. G. Mitigation of Water Fouling: Technology Status and Challenges. *Adv. Heat Transfer* **1998**, *31*, 431–474.
- (58) Camino, C.; Lomakin, S. M.; Lazzari, M. Polydimethylsiloxane Thermal Degradation Part 1. Kinetic Aspects. *Polymer* **2001**, *42* (6), 2395–2402.
- (59) Edwards, T. Cracking and Deposition Behavior of Supercritical Hydrocarbon Aviation Fuels. *Combust. Sci. Technol.* **2006**, *178* (1–3), 307–334.
- (60) Wohlwend, K.; Maurice, L.; Edwards, T.; Striebig, R.; Vangsness, M.; Hill, A. Thermal Stability of Energetic Hydrocarbon Fuels for Use in Combined Cycle Engines. *J. Propul. Power* **2001**, *17* (6), 1258–1262.
- (61) Aparicio, M.; Jitianu, A.; Rodriguez, G.; Degnah, A.; Al-Marzoki, K.; Mosa, J.; Klein, L. C. Corrosion Protection of Aisi 304 Stainless Steel with Melting Gel Coatings. *Electrochim. Acta* **2016**, *202*, 325–332.
- (62) Castro, Y.; Ferrari, B.; Moreno, R.; Durán, A. Coatings Produced by Electrophoretic Deposition from Nano-Particulate Silica Sol-Gel Suspensions. *Surf. Coat. Technol.* **2004**, *182* (2–3), 199–203.
- (63) Shi, Z.; Xiao, Y.; Qiu, R.; Niu, S.; Wang, P. A Facile and Mild Route for Fabricating Slippery Liquid-Infused Porous Surface (Slips) on CuZn with Corrosion Resistance and Self-Healing Properties. *Surf. Coat. Technol.* **2017**, *330*, 102–112.
- (64) Wang, P.; Zhang, D.; Lu, Z.; Sun, S. Fabrication of Slippery Lubricant-Infused Porous Surface for Inhibition of Microbially Influenced Corrosion. *ACS Appl. Mater. Interfaces* **2016**, *8* (2), 1120–1127.
- (65) Watkinson, A.; Martinez, O. Scaling of Heat Exchanger Tubes by Calcium Carbonate. *J. Heat Transfer* **1975**, *97* (4), 504–508.
- (66) Sheikholeslami, R.; Watkinson, A. Scaling of Plain and Externally Finned Heat Exchanger Tubes. *J. Heat Transfer* **1986**, *108* (1), 147–152.
- (67) Melo, L.; Bott, T. R.; Bernardo, C. A. *Fouling Science and Technology*; Springer Science & Business Media, 2012; Vol. 145.
- (68) Curran, J. A.; Clyne, T. W. The Thermal Conductivity of Plasma Electrolytic Oxide Coatings on Aluminium and Magnesium. *Surf. Coat. Technol.* **2005**, *199* (2), 177–183.
- (69) Ge, Z.; Cahill, D. G.; Braun, P. V. Thermal Conductance of Hydrophilic and Hydrophobic Interfaces. *Phys. Rev. Lett.* **2006**, *96* (18), 186101.
- (70) Zheng, Q. S.; Yu, Y.; Zhao, Z. H. Effects of Hydraulic Pressure on the Stability and Transition of Wetting Modes of Superhydrophobic Surfaces. *Langmuir* **2005**, *21* (26), 12207–12212.
- (71) Forsberg, P.; Nikolajeff, F.; Karlsson, M. Cassie-Wenzel and Wenzel-Cassie Transitions on Immersed Superhydrophobic Surfaces under Hydrostatic Pressure. *Soft Matter* **2011**, *7* (1), 104–109.
- (72) Cha, H.; Vahabi, H.; Wu, A.; Chavan, S.; Kim, M.-K.; Sett, S.; Bosch, S. A.; Wang, W.; Kota, A. K.; Miljkovic, N. Dropwise Condensation on Solid Hydrophilic Surfaces. *Science Advances* **2020**, *6* (2), No. eaax0746.
- (73) Jones, E. G.; Balster, L. M.; Balster, W. J. Quantitative Evaluation of Jet-Fuel Fouling and the Effect of Additives. *Energy Fuels* **1995**, *9* (5), 906–912.